Nano Energy 134 (2025) 110556

Contents lists available at ScienceDirect

Nano Energy

journal homepage: www.elsevier.com/locate/nanoen

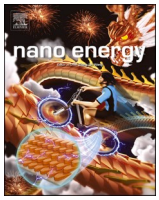

Full paper

The role of Li doping in layered/layered $Na_xLi_yNi_{0.4}Fe_{0.2}Mn_{0.4}O_2$ intergrowth electrodes for sodium ion batteries

Eric Gabriel [a], Pengbo Wang [b], Kincaid Graff [a], Shelly D. Kelly [d], Chengjun Sun [d], Changjian Deng [a], Inhui Hwang [d], Jue Liu [e], Cheng Li [e], Sarah Kuraitis [a], Jehee Park [f], Eungje Lee [f], Angel Conrado [a], Julie Pipkin [a], Max Cook [a], Stephanie McCallum [a], Yingying Xie [f], Zonghai Chen [f], Kamila M. Wiaderek [d], Andrey Yakovenko [d], Yang Ren [d], Yuming Xiao [d], Yuzi Liu [c], Elton Graugnard [a], Yan-Yan Hu [b,g,h,*], Dewen Hou [a,c,**], Hui Xiong [a,***]

[a] Micron School of Materials Science and Engineering, Boise State University, Boise, ID, 83725, USA
[b] Department of Chemistry and Biochemistry, Florida State University, Tallahassee, FL 32306, USA
[d] X-ray Science Division, Argonne National Laboratory, Argonne, IL 60439, USA
[e] Neutron Scattering Division, Oak Ridge National Laboratory, Oak Ridge, TN 37830, USA
[f] Chemical Sciences and Engineering Division, Argonne National Laboratory, Lemont, IL 60439, USA
[c] Center for Nanoscale Materials, Argonne National Laboratory, Argonne, IL 60439, USA
[g] Materials Science and Engineering Program, Florida State University, Tallahassee, FL 32310, USA
[h] Center of Interdisciplinary Magnetic Resonance, National High Magnetic Field Laboratory, Tallahassee, FL 32310, USA

ARTICLE INFO

Keywords:
Sodium ion batteries
Positive electrodes
Intergrowth
Layered oxides
Lithium doping
Surface coating

ABSTRACT

The layered $NaTMO_2$ (TM = Ni, Fe, Mn) materials with the O3-type structure are attractive as positive electrodes for sodium ion batteries because of their high theoretical capacity. Additionally, Li doping in these materials has been shown to offer substantial enhancements to their electrochemical properties by promoting the formation of intergrowth structures, which intimately integrate the substituent phases. However, the influence of the specific Li content on the structural and electrochemical properties of the intergrowth materials requires investigation. Systematic variation of Li content in $Na_xLi_yNi_{0.4}Fe_{0.2}Mn_{0.4}O_2$ (NFM-Li_y) was conducted to identify the role of Li in modification of the intergrowth structure and electrochemical performance. Li contents of 0.15 and greater generate a layered/layered Na-O3/Li-O'3 intergrowth structure. ^{7}Li and ^{23}Na solid-state nuclear magnetic resonance and x-ray absorption spectroscopy identify that when the total solubility for alkali ions in the layered structure is exceeded, Li continues to form the Li-O'3 phase while the excess Na forms residual sodium compounds such as Na_2O. Higher Li content is associated with improved capacity retention in the initial cycles from the superior stability of the mechanically linked Na-O3/Li-O'3 structure that suppresses the P3 to OP2 phase transition during charge. However, high Li contents are associated with increased rates of parasitic side reactions that reduce long-term cycling stability. These side reactions are connected to the instability of the cathode-electrolyte interphase, which can be partially mitigated by atomic layer deposition (ALD) coating with alumina, which significantly enhances the capacity retention and Coulombic efficiency. Overall, we find that the layered/layered Na-O3/Li-O'3 intergrowth structure is able to provide structural stability and suppress undesired phase transformations but is overwhelmed by the increased reactivity of the surface if not protected by surface coating.

* Corresponding author at: Department of Chemistry and Biochemistry, Florida State University, Tallahassee, FL 32306, USA.
** Corresponding author at: Micron School of Materials Science and Engineering, Boise State University, Boise, ID 83725, USA.
*** Corresponding author.
E-mail addresses: hu@chem.fsu.edu (Y.-Y. Hu), houd@anl.gov (D. Hou), clairexiong@boisestate.edu (H. Xiong).

https://doi.org/10.1016/j.nanoen.2024.110556
Received 18 April 2024; Received in revised form 6 December 2024; Accepted 6 December 2024
Available online 7 December 2024

1. Introduction

Sodium ion batteries (SIBs) are a promising candidate for large-scale energy storage applications because they can achieve competitive energy and power density compared to lithium-ion batteries while utilizing more abundant elements such as Na and Fe [1]. Considerable efforts have been made to develop positive electrode materials for SIBs, with the layered transition metal oxides (LTMOs) emerging as one of the most promising candidates for commercialization [1–4]. Among the different LTMO structures, the O3 type materials (according to the classification scheme of Delmas) [5] are desirable for practical applications because of their high sodium content (Na/TM ~ 1), which affords a high theoretical capacity. However, these materials often lack the necessary stability, energy density, or power density to meet the demands of practical applications.

The combination of multiple LTMO structures has been demonstrated to provide a number of benefits as a result of the synergistic effect of their different properties [2,6]. Compared to their single-phase counterparts, O3/P2 intergrowth structures often demonstrate both superior cycling stability and capacity retention at high rates [7–14]. For example, systematic variation of the Na content and transition metal composition in $Na_xMn_yNi_{1-y}O_2$ found that O3/P2 intergrowths could be prepared between $0.75 < x < 0.95$ with $y = 0.6$ [8]. The phase ratio could be tuned by further substitution of Mn with other elements (Cu, Fe, Ti), resulting in improved capacity retention and air stability[8]. $Na_x[Ni_{0.2}Fe_{x-0.4}Mn_{1.2-x}]O_2$ (x = 0.7–1.0) showed O3/P2 intergrowths for $x < 0.8$ [9]. The optimized material ($x = 0.78$) displayed an excellent capacity retention of 90 % after 1500 cycles and maintained 66 % of its capacity at a high 10 C rate [9]. $Na_{1-x}Li_xNi_{0.5}Mn_{0.5}O_2$ displays either a combination of O3 and P2 phases ($x = 0.3$) or a single O3 phase ($x = 0$) [10]. O3/P2 $Na_{0.7}Li_{0.3}Ni_{0.5}Mn_{0.5}O_2$ maintained 95 % of its discharge capacity at a 150 mA/g current rate, while O3 $NaNi_{0.5}Mn_{0.5}O_2$ only retained 60 % [10].

The ability of Li doping to generate layered intergrowth structures between Na-rich and Li-rich phases has also been noted. Lithium's unique combination of small size (comparable to 3d TMs) and 1 + valence allows it to occupy both the TM layer and/or the alkali layer [10,15,16]. Corresponding to its low ionic potential compared to the TM elements, and high ionic potential compared to Na^+, Li^+ is expected to promote O3-type structures regardless of its position in the layered structure [17]. Li excess layered oxide electrode materials (where Li/TM > 1), where Li partially occupies the TM layer (e.g., Li_2TMO_3 or equivalently in the layered notation, $Li[Li_{1/3}Mn_{2/3}]O_2$), have been the subject of considerable investigation for use in lithium ion batteries [18]. Unfortunately, similar structures do not typically form in the Na based LTMOs with the 3d TM elements due to the large size difference between Na and the 3d TM elements. However, we note the previous observations of LTMO structures with both Li and Na ($NaLi_{1/3}Mn_{2/3}O_2$ and $NaLi_{1/3}Ti_{1/6}Mn_{1/2}O_2$) [16,17,19] could allow the design of alkali excess structures. $Na_{0.87}Li_{0.25}Ni_{0.4}Fe_{0.2}Mn_{0.4}O_2$ was previously reported to have improved properties compared to the Li-free material with the O3 structure and does not rely on anion redox for charge compensation [16].

Here, we systematically investigate the role of Li content in the alkali excess $Na_xLi_yNi_{0.4}Fe_{0.2}Mn_{0.4}O_{2+\delta}$ system ($x + y > 1$). We identify that an Na-O3/Li-O'3 intergrowth structure can be formed with sufficient level of Li doping, which can promote the structural stability via the mechanical coupling between the two phases. However, the degree of alkali excess that can be accommodated by the layered/layered structure is limited and the higher Li content can promote increased side-reactions that ultimately harm the stability of the electrode over long term cycling. The surface reactivity can be managed to an extent by coating with alumina, allowing the benefits of the intergrowth structure to be more completely realized.

2. Results and discussion

2.1. Structural characterization

2.1.1. X-ray and neutron diffraction

Samples with composition $Na_xLi_yNi_{0.4}Fe_{0.2}Mn_{0.4}O_{2+\delta}$ (NFM-Li_y; x~0.97–1.0, y = 0–0.34) were prepared by solid state reaction from a combination of transition metal hydroxide (prepared by coprecipitation) with appropriate quantities of sodium and lithium carbonates. Inductively coupled plasma mass spectroscopy (ICP-MS) was conducted to determine the overall composition (Table S1). The nominal Li composition is used for convenience in the following discussion. To investigate the influence of the Li content on the overall structure, we conducted synchrotron x-ray diffraction (XRD, Fig. 1a) and neutron powder diffraction (NPD, Fig. 1b). According to Rietveld refinement of the XRD patterns (shown for $Li_{0.00}$ and $Li_{0.30}$ in Figure S1, and detailed structure model and fitting results in Tables S2-S4), the undoped sample is composed predominately of an Na-O3 type layered structure (space group R-3m) with an interlayer distance of 5.33 Å, and a minor (2.4 wt %) NiO-like rock salt (space group Fm-3m) type impurity (Fig. 2a). Increased Li contents of 0.05 and 0.10 reduce the amount of the cubic NiO-like phase to 1.6 and 1.4 wt%, respectively, and NiO is fully eliminated at $Li_{0.15}$ and greater. As the Li content increases, the interlayer distance (c lattice parameter) of the Na-O3 phase gradually decreases by ~1.0 % to ~5.28 Å (Fig. 2b.), while the intraplanar distances (a lattice parameter) marginally increased by 0.05 % at most. The incorporation of isovalent Li^+ onto the Na^+ layer could explain the lattice parameter trend, as the smaller size of Li ions enables smaller interlayer distances without requiring oxidation of the transition metals that would induce an in-plane contraction. At Li contents of 0.15 and greater, the cubic NiO phase is eliminated and the intensity of the (001) peak of an Li-O'3 phase (Li-rich O3 with monoclinic distortion, space group C 2/m) increases in the XRD patterns with a small interlayer distance ($c\ \sin(\beta)$) of ~4.5–4.8 Å. A similar cubic-to-layered transition is known to occur in the $NiO/LiNiO_2$ series [20,21], as separation of Li and TM ions occurs due to the steric effect of the smaller TM ions and larger Li ion at sufficiently high Li concentrations. The linear decrease of the NiO unit cell a lattice parameter (Fig. 2c) and volume (Fig. 2d) from Li 0.00–0.10 suggests the incorporation of Li into the NiO-like phase a solid solution manner ($Li_xTM_{1-x}O$) in this range. The weight fraction of the secondary phase increases with Li content while the unit cell volume decreases.

The NPD patterns of the Li doped samples demonstrate features at ~3.00, 3.26, 3.44, 3.78, 3.88, and 4.35–4.46 Å that are not present in the XRD patterns, which suggests the presence of cation ordering [22,23]. The x-ray scattering power of the transition metals is very similar while Li is very weak, allowing for Li to be distinguished by XRD from the TM elements but not the TM elements from each other. The absence of these features in the XRD patterns suggests that the cation ordering is not related to Li and more likely arises from the TM elements. On the other hand, the varied coherent neutron scattering lengths (b_{Coh}) of each cation are −2.22, −3.73, 9.45, and 10.3 fm for ^{7}Li, Mn, Fe, and Ni, respectively. Consequently, NPD provides the ability to identify the presence of TM ordering, particularly the ordering of Mn or Li from Fe or Ni. The presence of Li^+/vacancy ordering is an alternative possibility [24]. However, considering the high in-plane mobility and weak interaction expected for Li^+ atoms in different layers, multicomponent TM composition, and the relatively low neutron scattering power of ^{7}Li, we believe this to be less probable. Therefore, we conclude that these features arise from the presence of superlattice ordering between Mn and Ni/Fe. The additional features in the NPD patterns increase in strength with the fraction of the Li-O'3 phase and are absent in the $Li_{0.00}$ sample and also become faintly resolved in the $Li_{0.10}$ sample, before the Li-O'3 phase becomes identifiable in the XRD. The superlattice associated with honeycomb-like intralayer ordering of cations on the TM layer known to occur in O'3-$Li[Li_{1/3}Mn_{2/3}]O_2$ [25,26] or O3-$NaLi_{1/3}Ti_{1/6}Mn_{1/2}O_2$ [17]

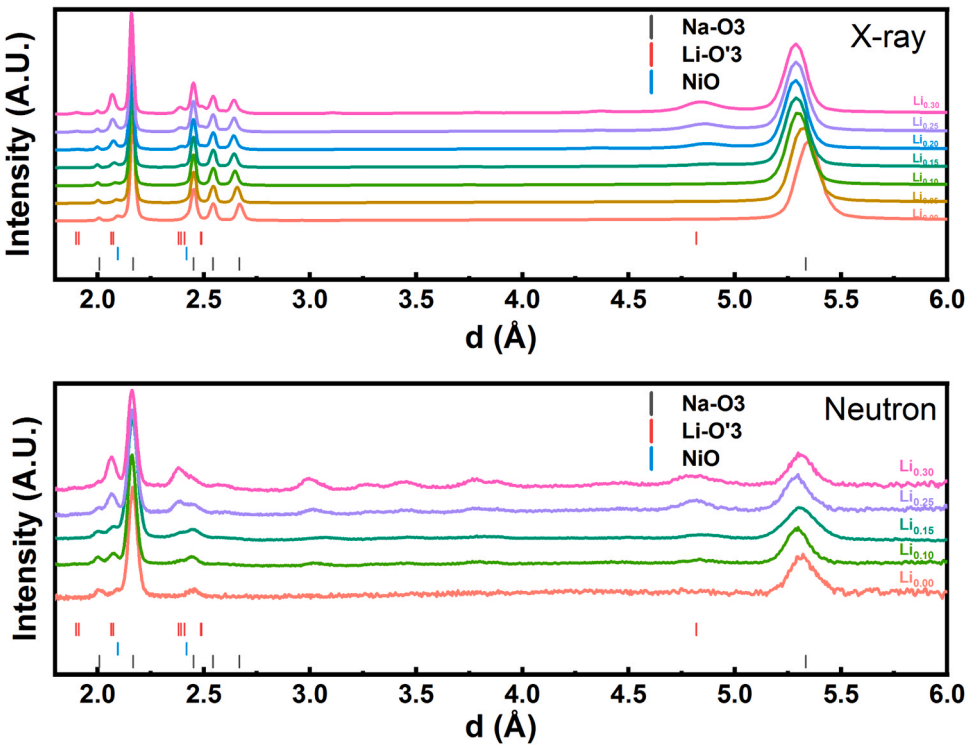

Fig. 1. a) Synchrotron x-ray diffraction (λ = 0.1173 Å) and b) Neutron powder diffraction of Li 0–0.30 samples. The peak positions of Na-O3 and NiO are indicated for the $Li_{0.00}$ pattern, and the Li-O'3 positions are indicated for the $Li_{0.30}$ pattern.

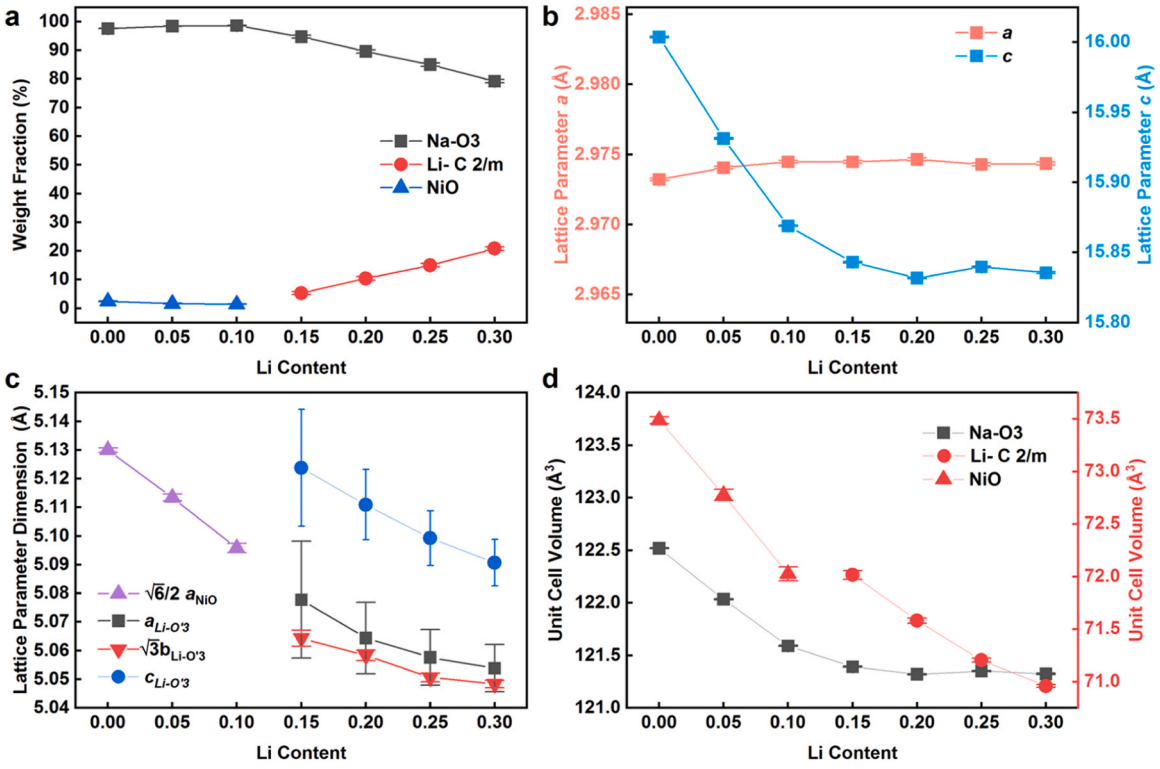

Fig. 2. Values of fitted parameters in the Rietveld refinements of the XRD data as a function of Li content. The error bars represent the standard uncertainties of the refined values. a) Weight fractions of each phase. b) Lattice parameters of the Na-O3 phase. c) Lattice parameters of the Li-O'3 and NiO phases. a_{NiO} and $b_{Li\text{-}O'3}$ are scaled to indicate equivalent distances between the structures. d) Unit cell volumes of each phase.

and related compounds may be present, considering the presence of the (1/3 0 0) superlattice peak of the Na-O3 phase (4.46 Å, in the R-3m structure) and equivalent (0 2/3 0) peak of the Li-O'3 phase (4.37 Å in the C2/m structure). The other superlattice reflections between 3 and 4 Å cannot be unambiguously assigned but may also reflect the intra-planar ordering. Additionally, Fe has a tendency to mix onto the Li layer in Li-based layered oxides [27] and the refinement suggests 20–25 % occupancy of TM ions on the Li layer of the Li-O'3 phase, which could be related with the cation ordering. We were not able to identify a super-structure that could reliably index the observed peaks. Overall, lithium doping can promote the shrinkage of the Na-O3 and Li-O'3 unit cells, the formation of the Li-O'3 phase, and the ordering between the Mn and Ni/Fe ions.

2.1.2. Electron microscopy

The degree of integration and local structural properties of the Na-O3 phase and Li-O'3 phase are also of considerable interest. We utilized high-resolution transmission electron microscopy (HR-TEM) to investigate both $Li_{0.20}$, $Li_{0.25}$, and $Li_{0.30}$ samples (Fig. 3 and Figure S2). At $Li_{0.25}$ and $Li_{0.30}$ there is direct integration along the layering direction of well-crystallized Na-O3 and Li-O'3 phases with distinct interlayer spacings that produce clearly separated spots in the selected area electron diffraction (SAED) patterns (Fig. 3b). A low magnification view of Fig. 3c and an additional representative particle cluster and its SAED pattern are given in Figure S2a-d. Similar imaging of the Na-O3/Li-O'3 interface in $Li_{0.25}$ is given in Figure S2e-h. At the lower Li content of 0.20, integrated domains of each phase are also evident, but there is considerable disorder of the layered structures. These samples indicate that increasing Li content may also promote the crystallinity of the Li-O'3 phase, which may further alter its role in the material during electrochemical cycling. While ordered and disordered domains can be found in the HR-TEM for both Li contents, the increased crystallinity of the higher Li content samples on average is supported by the Rietveld refinement results according to their larger average domain size (according to the Scherrer broadening) [28–30].

2.1.3. X-ray absorption spectroscopy

In order to investigate the influence of the composition on the local structure and oxidation states of each transition metal we performed synchrotron x-ray absorption spectroscopy (XAS). The x-ray absorption near-edge structure (XANES) region of the XAS spectra for each transition metal in the pristine materials identified no change in the transition metal oxidation states based on the insignificant change in the K-edge energies with different Li contents (Fig. 4a-c), with the Ni^{2+}, Fe^{3+}, and Mn^{4+} as the predominant states based on their similarity to reference compounds (NiO, Fe_2O_3, MnO_2). This result suggests that Li^+ doping is

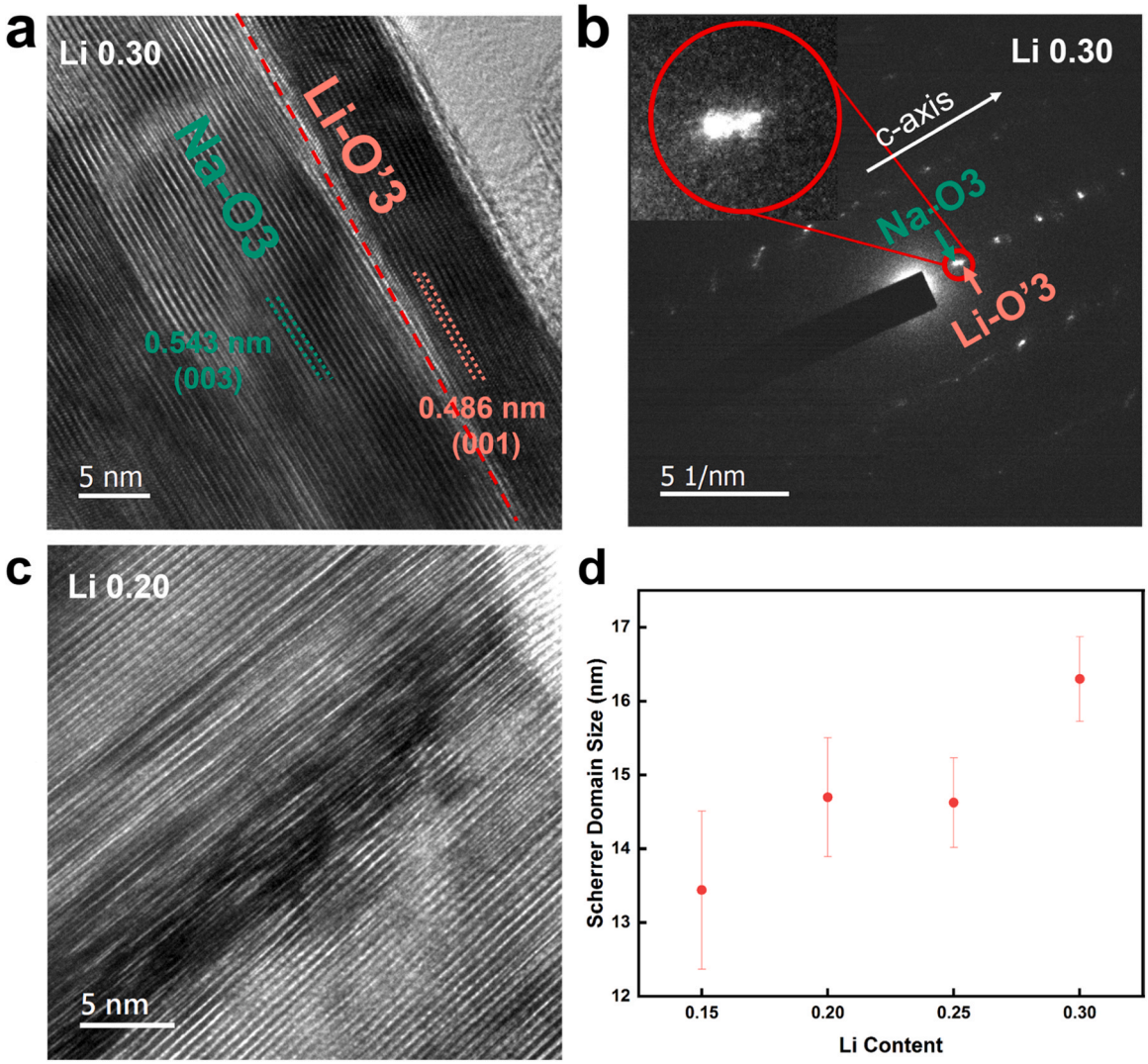

Fig. 3. a) HR-TEM of $Li_{0.30}$. b) SAED pattern of region shown in panel a. c) HR-TEM of $Li_{0.20}$. d) Domain size of the Li-O'3 phase determined from refinement of the XRD patterns.

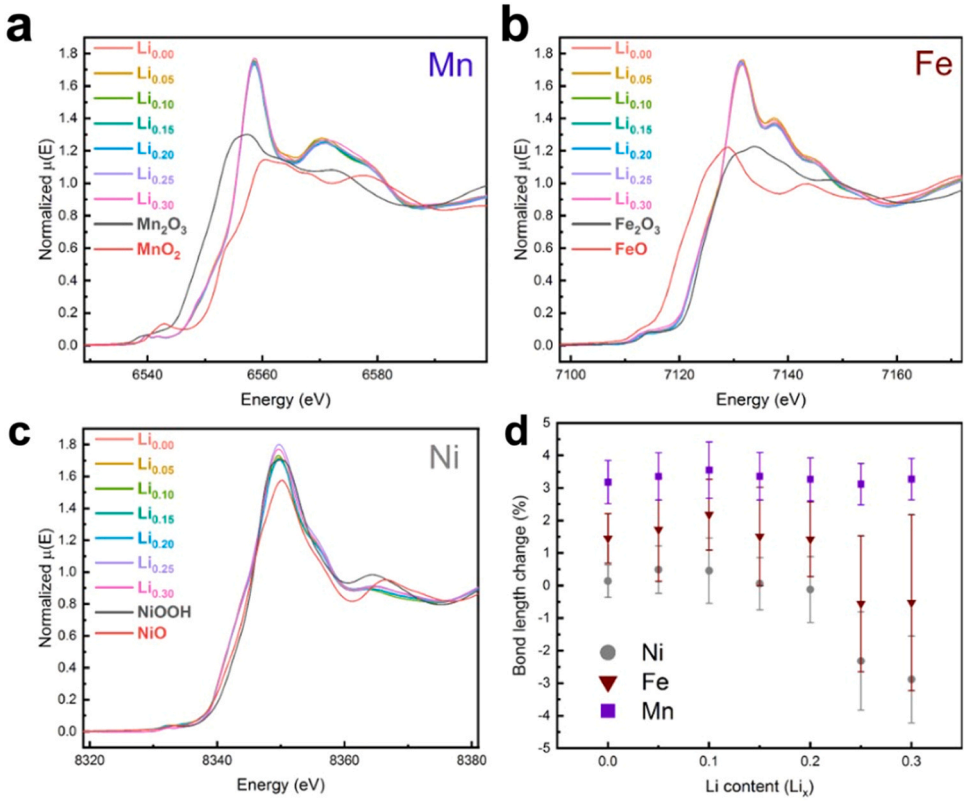

Fig. 4. K-edge XANES of a) Mn, b) Fe, and c) Ni in the NFM-Li_y system shows no significant shift with changing Li content. d) EXAFS fit parameter α_{TM3} that corresponds to interlayer distance as a function of Li content.

primarily compensated by the formation of some secondary phase such as Na_2O or Li_2O, and that the solubility of the alkali ions ((Na+Li)/TM) is not significantly larger than 1. This also suggests that the Li and Na within the layered structures predominantly occupy the alkali layer. A detailed discussion of the charge compensation mechanism is given in the supporting information (Note S1).

We further investigated the extended x-ray absorption fine structure region (EXAFS) of the XAS spectra for each TM to observe how their local structure can be related to the long-range structure identified by XRD and NPD. The Fourier transformed EXAFS spectrum was fitted between 1 and 6 Å (using $k = 3 - 9.5$ Å^{-1}) in order to capture both the intralayer and interlayer structure. The similarity between the Na-O3 phase and Li-O'3 phase allows a single structure model to fit both structures simultaneously with parameters that represent an average of both phases. This approach allows a good fit to the data with a small number of variables to ensure the significance of each model parameter and avoid overfitting. The scattering paths are assigned a fractional path length change parameter (α) and common parameter for the mean square displacement about half the path length (σ) that is shared for all scattering paths contained within equivalent TMO_6 or NaO_6 octahedra. Visualization of the structure model and the detailed fitting procedures and results are provided in Figure S3 and S4, and Tables S5–7. The parameters associated with the in-plane octahedra with the TM atom distances of a, $\sqrt{3}a$, and $2a$ and the NaO_6 octahedra show no significant trends with the Li content. However, the α term associated with the interlayer bond lengths (α_{TM3}) shows significant dependence on the Li content (Fig. 4d). As the Li content increases, there is a significant decrease in α_{TM3} for both Ni and Fe, but not Mn. This suggests that Ni and Fe become closer to their neighboring layers as the Li content increases. The c lattice parameter decreases by 1 % or less in both the Na-O3 and Li-O'3 phases based on the Rietveld refinements. The magnitude of this interlayer path length change (α_{TM3}) is significantly greater than 1 %. This suggests that the decrease of α_{TM3} for Ni and Fe is associated with their increasing concentration in the Li-O'3 phase because of the considerably smaller interlayer distance (~10–15 % for $Li_{0.15–0.30}$ compared to $Li_{0.00}$) in the Li-O'3 structure. The electrochemical activity of Ni and Fe may be reduced as a result of being in an Li-rich structure compared to the Na-rich structure since Fe tends to reduce the capacity of Li-based layered oxides [27]. Further, Li-based layered oxides typically exhibit higher redox potentials compared to their Na-based equivalents [31]. Consequently, the redox activity of Ni and Fe in the Li-O'3 phase may be partially suppressed in the fixed potential window.

2.1.4. *Solid-state nuclear magnetic resonance*

To understand how the local environment of the Na and Li is altered by the changing composition, we conducted solid state nuclear magnetic resonance measurements (ssNMR) to probe both ^{23}Na and ^{7}Li. The ^{7}Li ssNMR spectra of Li 0.10, 0.20, and 0.25 demonstrate a single broad resonance that represents the overlap of numerous local environments for Li. As reference, we prepared a sodium-free sample with nominal composition $Li_1Ni_{0.4}Fe_{0.2}Mn_{0.4}O_2$ (Li_1Na_0) that displays a very similar ^{7}Li NMR spectrum to the samples with both Na and Li. Typical values of the ^{7}Li shift for Li on the alkali layer in layered structures are between 0 and 1000ppm, and the main resonances of $LiFeO_2$, $LiNiO_2$, and $LiMnO_2$ are found at 1000 ppm or lower [32,33], so we assign the largest component at ~1000ppm and the two others at lower shifts to Li in the Li layer. The component of the Li_1Na_0 sample with central position at roughly 1500 ppm likely arises from Li coordinated by 6 Mn^{4+} ions in the TM layer as observed in $LiNi_{0.5}Mn_{0.5}O_2$ and $Li[Li_{1/3}Mn_{2/3}]O_2$ [34,35]. This assignment is supported by the presence of small superlattice peaks between 4.0 and 4.3 Å in the synchrotron XRD pattern of Li_1Na_0 (Figure S1c) and could explain the weak signal seen in the same range for $Li_{0.20}$ and higher Li content samples. Similarly, the resonance around 1300 ppm could arise from similar configurations of Li on the TM layer but with slightly altered coordination (e.g., $LiMn_5TM$). However, we note that the Rietveld refinement suggests a significant occupancy of

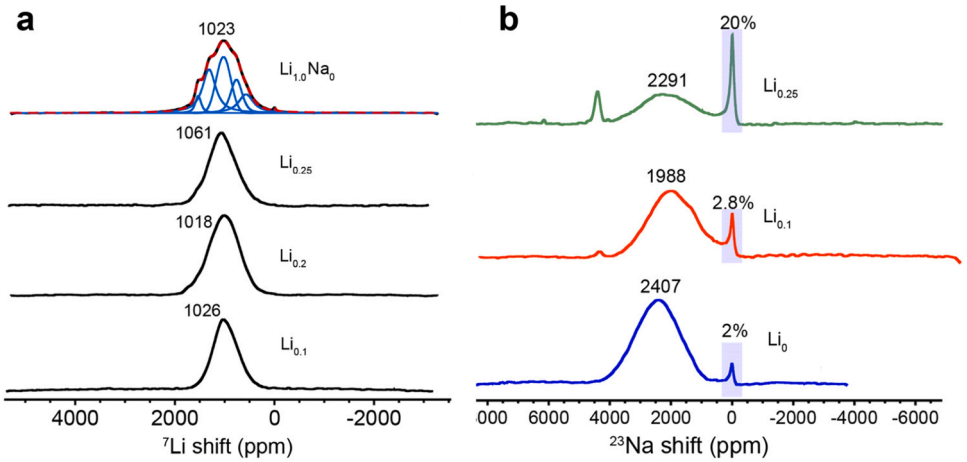

Fig. 5. a) ^{7}Li and b) ^{23}Na ssNMR of pristine samples with varied composition. The percentages indicate the contribution of the highlighted feature to the integrated intensity.

transition metals (0.22–0.25) on the Li layer of the Li-O'3 phase that might contribute to different shifts than expected for purely separated Li and TM layers. These features at and above 1300 ppm are less prominent at $Li_{0.10}$ compared to $Li_{0.20}$ and $Li_{0.25}$ suggesting that higher Li content can weakly promote Li occupancy on the TM layer of the Li-O'3 phase. Overall, we conclude that Li is predominately located on the Li layer while a very small amount occupies the TM layer of the Li-O'3 phase only at high Li contents.

The ^{23}Na ssNMR demonstrates two distinct features (excluding the background peak from copper near 4000 ppm). The broad resonance centered between 2000 and 2400 ppm is associated with Na in various paramagnetic environments in the Na layer of the Na-O3 structure. The shift of the Na signal may be related to the change in lattice parameter of the Na-O3 phase as well as its change in composition as the Li-O'3 phase competes for transition metals (especially Ni and Fe as suggested by the EXAFS). The diamagnetic component near 0 ppm represents residual sodium compounds such as Na_2CO_3, Na_2O, or NaOH. Notably, the signal from the residual Na compound increases at higher Li contents. This

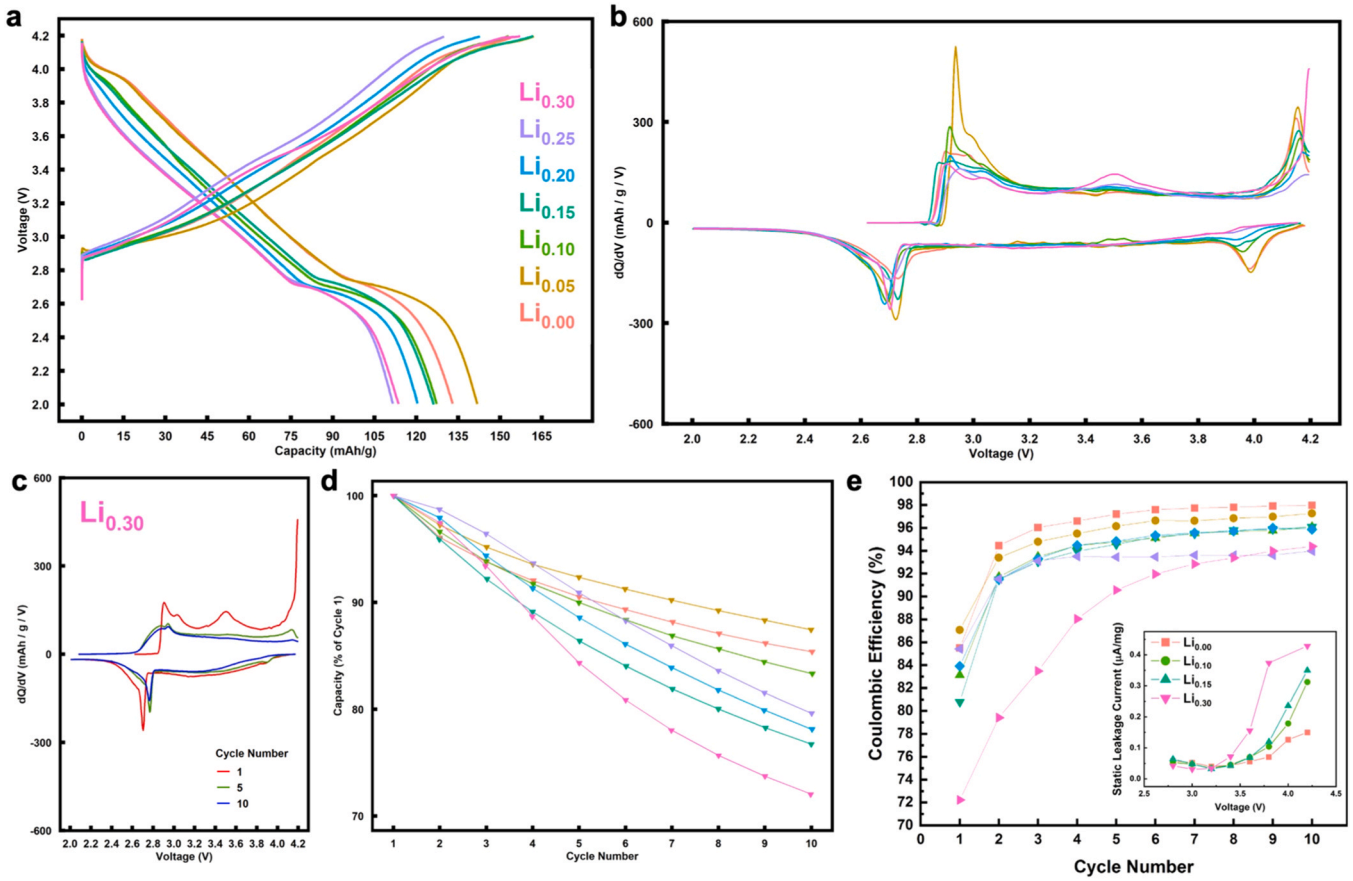

Fig. 6. a) First cycle voltage profiles of NFM-Li_y electrodes (CR2032 coin cells against Na metal with 1 M $NaPF_6$ in propylene carbonate at 15 mA/g). b) Differential capacity (dQ/dV) plot of panel a. c) Differential capacity over the first 10 cycles for $Li_{0.30}$. d) Coulombic efficiency trend over the first 10 cycles. e) High-precision static leakage current measurements between 2.8 and 4.2 V.

suggests that the overall solubility for alkali ions (Δ, see SI Note 1) in the $Na_xLi_yNi_{0.4}Fe_{0.2}Mn_{0.4}O_2$ framework is not significantly larger than 1, consistent with the XAS results. When excess Na and Li are present, the Li will be preferentially incorporated into the layered structures while the Na in excess of the solubility limit forms residual compounds such as Na_2O, in further agreement with XANES result. These species are poorly crystalline or amorphous and therefore do not manifest clearly in the diffraction patterns. These residual sodium species may also influence electrochemical performance. To evaluate the effect of these residuals and the overall structural changes prompted by Li doping, the electrochemical properties and structural changes during charge/discharge were systematically investigated (Section 2.2).

2.2. Electrochemical characterization

The first cycle voltage profiles (between 2 and 4.2 V vs Na/Na^+) obtained by galvanostatic cycling demonstrate a reduction in both the first-cycle charge and discharge capacities as the Li content increases beyond 0.05 (Fig. 6a). The changes in the electrochemical processes are evident in the comparison of the differential capacity analysis (dQ/dV, Fig. 6b). The capacity increase observed for $Li_{0.05}$ compared to $Li_{0.00}$ is primarily provided by the increase of the feature around 2.7 V/2.9 V in the discharge/charge, respectively. With further increase of Li content, the high-voltage plateau near 4.0–4.2 V is suppressed, and then a gradual decrease in capacity associated with the 2.7–2.9 V peak. The concentration of Ni and Fe suggested by the EXAFS measurements in the Li-O'3 phase may be partially responsible for the reduced capacity, since Li based layered oxides tend to have higher redox potentials than their Na based counterparts and Fe does not typically provide significant reversible capacity in Li based layered oxides (e.g., $LiFeO_2$)[36]. At higher Li contents, especially $Li_{0.30,}$ there are irreversible redox processes evident at 3.5 V and 4.2 V during charge that are not visible in the discharge. The process at 4.2 V is the primary contributor to the irreversibility beyond the first cycle, as shown in the dQ/dV of $Li_{0.30}$ over the first 10 cycles (Fig. 6c). The capacity retention over the first 10 cycles shows that the reversible discharge capacity over the first 2–4 cycles can be superior for the high Li content samples (0.20–0.30) compared to the lower levels of doping (0.0–0.10). However, a general trend of lower Coulombic efficiency for samples with higher Li content is observed over the first 10 cycles (Fig. 6e). We performed high-precision static leakage current measurements[37] (Fig. 6e inset) after 3 cycles that corroborate the trend of accelerated side reaction at higher Li contents which begin from progressively lower voltages. The average potential difference between charge and discharge in the first 10 cycles as well as the change of discharge capacity at low and high current (15 mA/g and 100 mA/g) indicate (Figure S5) that the $Li_{0.05}$ sample has superior Na^+ transport kinetics to $Li_{0.00}$. The polarization and capacity at higher rate gradually become worse with increasing Li content beyond $Li_{0.05}$, which is attributed to the surface degradation associated with the increasing side reaction. The electrochemical performance over the initial 10 cycles raises two key questions: What allows the high Li content samples to maintain their reversible discharge capacity in the first few cycles despite the high rate of side reaction? And why does the Li content influence the rate of the side reaction?

2.2.1. The role of Fe in charge compensation

We previously established that the long-term capacity retention of $Na(Ni_{0.5}Mn_{0.5})_{1-x}Fe_xO_2$ electrodes is likely related to an interaction between Ni and oxidized Fe that harms the reversibility of the Ni redox couple over long-term cycling [38]. Considering this, we performed resonant and non-resonant Fe K_β x-ray emission spectroscopy ((R)XES) [39] and high-resolution fluorescence detected XANES [40] (HERFD--XANES) to identify the influence of Li on the electronic structure of Fe (Figure S6-S8). A detailed discussion of the RXES and HERFD-XANES results is given in the Supporting Information (SI Note 2). No detectable differences in the $K_{\beta1,3}$ XES spectra of the pristine materials or charged $Li_{0.00}/Li_{0.25}$ (4.2 V) were observed (Figure S6). Further, the features associated with the $3d^4$ spin-state of Fe^{4+} did not appear in the HERFD-XANES spectra of $Li_{0.00}$, $Li_{0.10}$, $Li_{0.25}$, and several other Fe-rich LTMOs (Figures S7 and S8). Overall, we conclude that change of the electronic structure of Fe is not a major factor in the differing electrochemical performance between the low and high Li content samples. In general, the Fe redox activity in Na LTMOs appears to result from a loss of the shared electron density between overlapped Fe-3d and O-2p orbitals rather than a purely ionic Fe^{3+}/Fe^{4+} transition or oxygen redox.

2.2.2. Long-range structural evolution during charge/discharge

Considering that the majority of Fe is Fe^{3+} in these samples, and Fe migration resulting from the lack of octahedral site preference of Fe^{3+} has been suggested as a driving force for phase transformation in $NaNi_{0.4}Fe_{0.2}Mn_{0.4}O_2$, the phase transformation behavior during cycling may be a critical factor in the electrochemical reversibility of these materials [41,42]. The suppression of the high voltage plateau in the high Li content samples suggests the possibility of a different phase transformation pathway compared to the low Li content materials. To examine the structural evolution during the first cycle, operando XRD was conducted on the $Li_{0.00}$, $Li_{0.10}$, and $Li_{0.25}$ samples (Fig. 7 and S9). The lattice parameters and unit cell volume of the Na-O3 and related phases were determined by the Le Bail method (Figure S10 and S11) [43]. During the first charge of the undoped material, the structure undergoes a two-phase transition from O3 to P3 between 3.00 and 3.15 V, indicated by a characteristic increase in the (10−5)/(104) intensity ratio. The gradual shift of (003)/(006) to lower angle and the (10 *l*) peaks to higher angle indicates the interlayer distance increases as a result of Na^+ extraction while intraplanar distances decrease as TM ions oxidize. The P3 structure becomes unstable above 4.15 V as suggested by the decreased intensity of the (003) and (10 *l*) peaks. This is associated with a partial transition to an OP2-like phase, which has been shown previously to form during charge to 4.3 V in $NaNi_{0.4}Fe_{0.2}Mn_{0.4}O_2$ [42]. The transition toward the OP2 structure is further suggested by the decrease of the interlayer spacing above 4.15 V (Figure S11). In the subsequent discharge, this transition is only partially reversed with a fraction of the (006) peak remaining at same position as the fully charged state, and the remainder at higher angle than the pristine material. These irreversible changes signify the permanent expansion between layers. The accumulated irreversible OP2 phase transformation can explain the irreversible discharge capacity loss seen for the undoped sample.

The phase transformation of $Li_{0.10}$ over the first cycle is reversible (Figure S9) but it cannot avoid the partial P3→OP2 transformation also seen in $Li_{0.00}$. The decrease of the interlayer distances ($\Delta c/c_0$) for the Na-O3 phase at high state of charge (~85 and 90 %) associated with the OP2 transformation are −0.36 % and −0.16 % for $Li_{0.00}$ and $Li_{0.10}$, respectively. Upon discharge, $Li_{0.00}$ retains an irreversible 0.20 % decrease of the interlayer distance compared to its maximum value, while NFM-$Li_{0.10}$ only decreases by 0.04 %. This identifies that Li within the Na-O3 phase has a role in improving the reversibility of the P3→OP2 transformation but can still allow accumulation of the interlayer expansion.

The $Li_{0.25}$ material demonstrates clear differences in the phase transformation pathway of the Na-O3 phase (Fig. 7). A similar O3 to P3 transition and lattice expansion/contraction occurs in $Li_{0.25}$ as observed for $Li_{0.00}$ and $Li_{0.10}$ (Figures S10 and S11). However, the P3 to OP2 transition is completely suppressed, demonstrating the superior structural reversibility of the Na-O3 phase in the $Li_{0.25}$ sample. According to the Na content in the Na-O3 phase determined by the Rietveld refinement (~$Na_{0.92}$, Table S4), the Na occupancy in the Na layer does not change significantly as a function of Li content between $Li_{0.10}$-$Li_{0.30}$. Similarly, the lattice parameters of the Na-O3 phase change by less than 0.2 % between $Li_{0.10}$ and $Li_{0.25}$. This suggests the Na-O3 phases in $Li_{0.10}$ and $Li_{0.25}$ are largely similar, so the difference in their phase transformation results from the presence of the Li-O'3 phase.

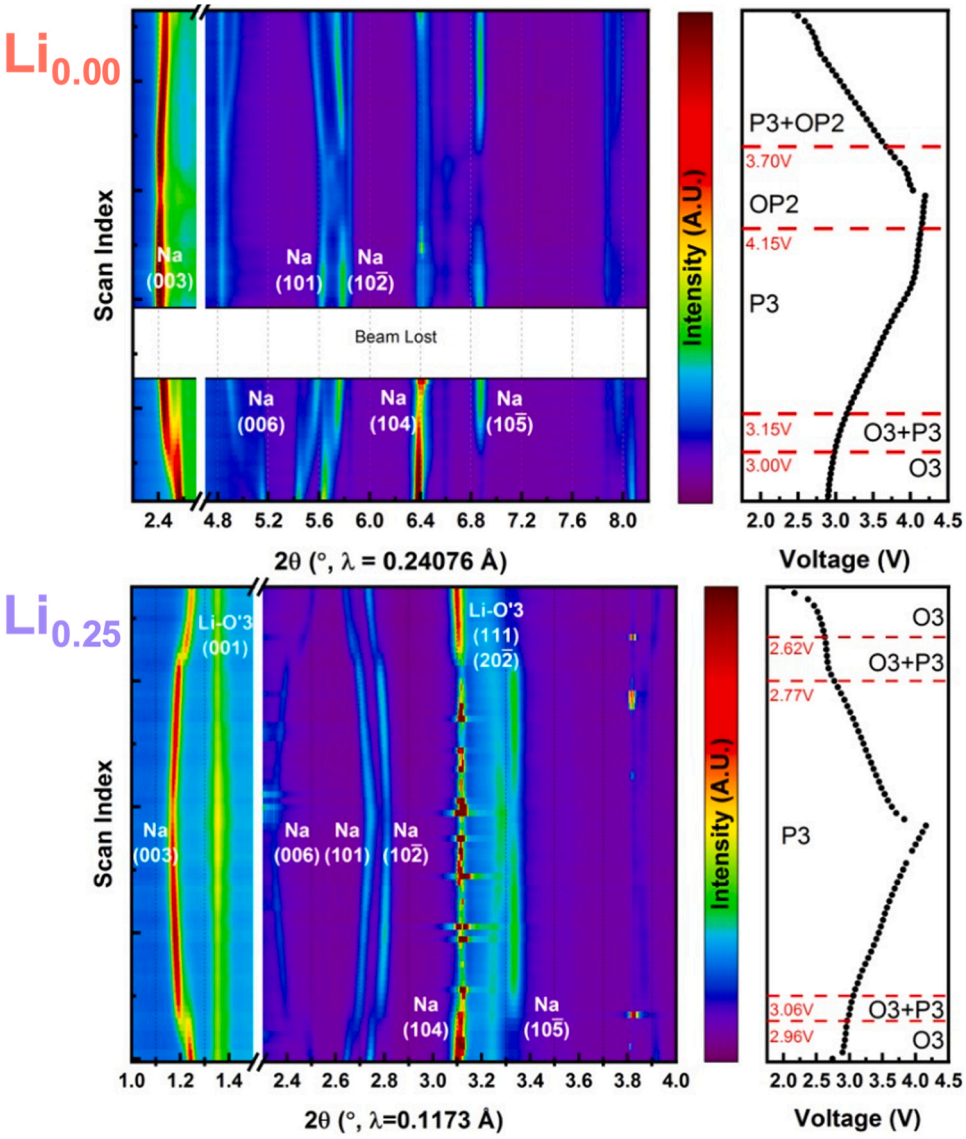

Fig. 7. Contour map of operando XRD data and the corresponding voltage profile obtained during the first cycle of $Li_{0.00}$ and $Li_{0.25}$. Blank range data omitted due to X-ray source instability.

In $Li_{0.25}$, the Li-O'3 phase undergoes no expansion or contraction of the interlayer distance as shown by the static position of the (001) peak (Fig. 7), which suggests little or no Li deintercalation occurs in this phase. However, there is a notable shift of the (111) and (20−2) peaks of the Li-O'3 phase to larger angles indicating a smaller value of the *a* lattice parameter. Given the intergrowth of the Na-O3 and Li-O'3 phases observed by HR-TEM, this peak shift could arise as a result of the mechanical coupling with the Na-O3 phase. As a result of their shared interface, the chemomechanical interaction between Na-O3 and Li-O'3 could suppress layer gliding necessary for the P3 to OP2 transition to occur. The strain energy associated with the interface interaction could shift the potential necessary to extract an equivalent amount of Na^+ to higher voltage, which might also contribute to the observed reduction in charge and discharge capacity at higher Li contents. Further, more frequent interfaces between the two phases would increase the average strength of the interface interaction. Consequently, greater quantities of the Li-O'3 phase within the Na-O3 matrix (as are observed at higher Li contents) would be expected to have a stronger stabilizing effect. Therefore, we conclude that mechanical reinforcement of the Li-O'3 phase can explain the superior stability of the $Li_{0.25}$ electrode in the first few cycles. The enrichment of the Na-O3 phase with Mn (Fig. 4d) and stronger cation ordering (Fig. 1) could be additional contributing factors to the suppression of the P3→OP2 transformation. Nonetheless, the issue of the parasitic side reaction remains.

2.2.3. *Parasitic side reaction and local alkali environment evolution*

The change of the individual alkali ion environment could reflect which environments are associated with the irreversible charge capacity of the side reactions. We collected *ex situ* ssNMR spectra of ^{23}Na and ^{7}Li from $Li_{0.25}$ at various states of charge to investigate their response to different states of charge (Fig. 8). The broad resonance associated with Na near paramagnetic TM ions in the Na-O3/P3 phases is suppressed by charging to 3 V or greater. The intensity reduction and shift of this resonance can be explained by the deintercalation of Na, the higher Na^+ mobility in the P-type structure, and the changing oxidation states of the TM elements (especially Ni) that will have fewer unpaired electrons to generate the paramagnetic interaction. The diamagnetic feature associated with the Na residues is also active during charge and discharge. These species may decompose at 4 V or greater based on the reduced intensity of the diamagnetic peak near 0 ppm but reappear after discharge to 2.7 V. The presence of the diamagnetic peak in the ^{23}Na spectrum at the 2.7 V discharged state suggests the formation of

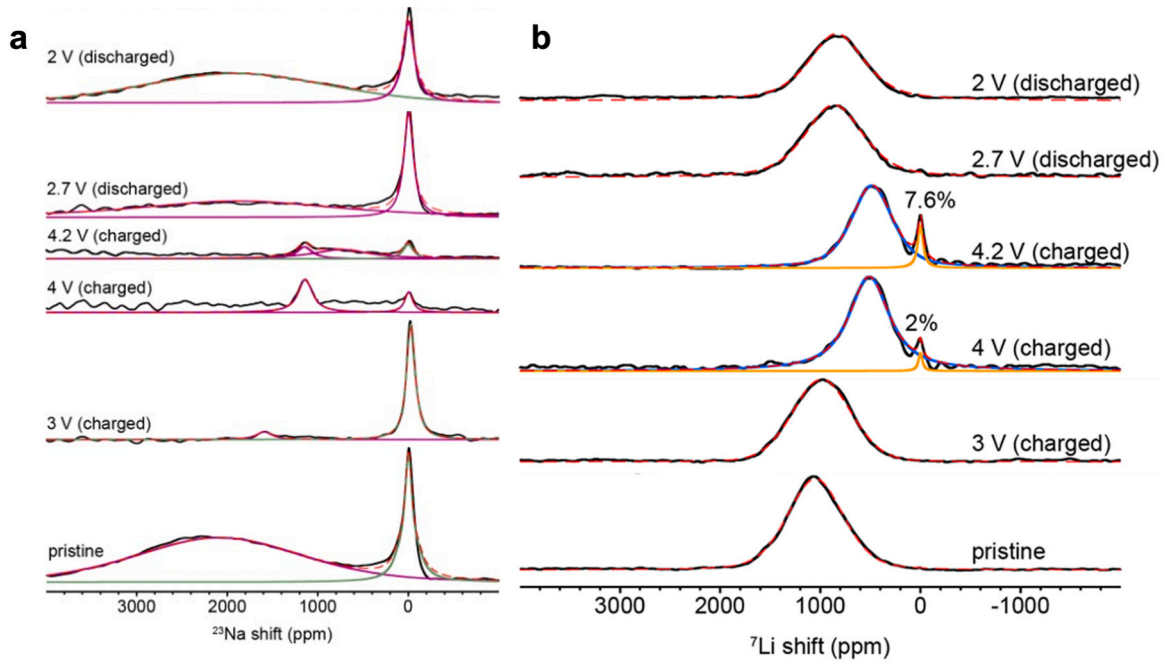

Fig. 8. Voltage-dependent changes in the alkali ion environment of $Li_{0.25}$ sample depicted through ssNMR spectra a) ^{23}Na and b) ^{7}Li.

cathode-electrolyte interphase (CEI) somewhere below 4 V is not entirely stable at 4 V and above. The peak position of the main resonance in the ^{7}Li ssNMR shifts from 1050 ppm in the pristine electrode to 480 ppm at 4.2 V. This may reflect the in-plane contraction observed in the operando XRD altering the bond lengths and angles. However, the normalized total intensity reflects a relatively small change during charging (-2.6 % at 4 V, −17.3 % at 4.2 V compared to pristine, normalized to the sample mass), which suggests the majority of Li remains intercalated. The connected nature of the Na-O3 and Li-O'3 phases might allow for mobile Li^{+} to migrate between the layered structures when the vacancy concentration in the Na-O3 phase becomes significant, which could further facilitate the stability of the P3 phase against the OP2 transition without requiring redox contribution from the Li-O'3 phase. This could further contribute to the shift of the resonance associated with Li in the alkali layer. During discharge, the main resonance partially reverses its position to 840 ppm at 2 V, suggesting some permanent distortion of the Li environment. At 4 V and 4.2 V, there is a substantial diamagnetic component (2.0 % and 7.6 % of the integrated intensity, respectively) to the ^{7}Li ssNMR near 0 ppm that is characteristic of Li environments with no unpaired electrons, such as Li_2O, Li_2CO_3, or LiF. This suggests the participation of Li in surface reactions that compose the CEI at high voltage. The small change of the normalized intensity between the 4.2 V charged state and 2 V discharged state and absence of the diamagnetic component suggests that the CEI is not stable, and the Li is not reintercalated, since the associated signal disappears during discharge. In any case, the ^{7}Li NMR indicates that the Li-O'3 phase is not inert against the electrolyte (1 M $NaPF_6$ in propylene carbonate) at 4 V or greater and must be a contributing factor to the side-reaction. Given the increasing rate of the side-reaction with increasing Li-content, the Li-O'3 phase must play a significant role in the worse Coulombic efficiency of the high Li content samples. The onset of higher static leakage current around 3.6 V in the $Li_{0.30}$ sample may then be associated with the decomposition of the CEI and subsequent electrolyte reaction. The long-term cycling stability of the electrodes is dominated by this effect (Fig. 9a). The capacity retentions correlate closely with the average coulombic efficiencies (over 500 cycles), which decrease monotonically with the Li content from 99.78 % to 99.13 % between $Li_{0.00}$ and $Li_{0.30}$.

2.2.4. *Surface protection by atomic layer deposition*

Considering the surface reactivity as the limiting factor in the performance of the higher Li content electrodes, we evaluated $Li_{0.00}$ and

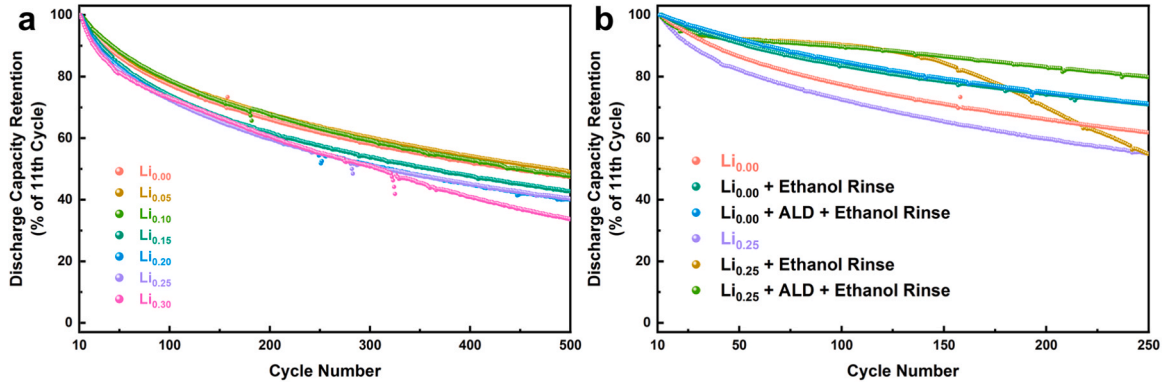

Fig. 9. a) % of discharge capacity retention at 100 mA g^{-1} after initial 10 low-rate cycles (shown in Fig. 6d) of the uncoated materials. b) Capacity retention of bare, ethanol rinsed, and ALD coated $Li_{0.00}$ and $Li_{0.25}$.

$Li_{0.25}$ with and without coating of alumina by atomic layer deposition (ALD). Surface protection provided by coatings of alumina with ALD have been shown to provide significant benefits in other layered oxide positive electrode materials for sodium ion batteries [44–47]. Four cycles of exposure to trimethylaluminum (TMA) followed by water were used to deposit the film, which nominally is expected to have a thickness of 0.5 nm according to the measured growth per cycle on a silica reference sample. The presence of Al in the sample after deposition was confirmed by energy dispersive x-ray spectroscopy.

Direct coating of the pristine $Li_{0.25}$ powder yielded substantial improvements in capacity retention and Coulombic efficiency with the alumina coating (Figure S12) for short term cycling. The coated sample retained 94.8 % of its maximum discharge capacity while the bare material only maintained 83.6 % after 30 cycles. An average Coulombic efficiency of 98.9 % over 30 cycles for the coated $Li_{0.25}$ suggests the superior stability of the alumina surface compared to 97.3 % for the bare material. Despite a slightly reduced maximum discharge capacity, 8.2 mAh g^{-1} less than the bare material, the coated $Li_{0.25}$ provides more discharge capacity than the bare material after 23 cycles. However, this enhanced stability could not be maintained over extended cycling after an abrupt decrease in Coulombic efficiency and accelerated capacity fading beyond 30 cycles. This is attributed to the incomplete coverage and/or finite protection of the surface provided by the coating. Considering the observed presence of residual sodium species, there may be regions of the surface that are not protected by the coating. When the sodium residuals decompose, similar surface degradation processes as in the bare material may occur.

With this possibility in mind, the effect of preparing the surface prior to coating with an ethanol rinsing step was evaluated (Fig. 9b). Ethanol rinsing has previously been shown to remove surface impurities and improve the air stability [48]. Both ethanol rinsing and ALD coating (after rinsing) are found to have beneficial effects on the long-term cycle stability. The capacity retention of the undoped material after 250 cycles improves from 61.3 % to 70.7 % after ethanol rinsing. The further coating of the undoped material by ALD results in no significant improvement in capacity retention (70.7 % at 250 cycles), suggesting good surface stability in the undoped material. Therefore, the previously demonstrated structural instability of the undoped material is still the primary cause of the capacity decay.

Similarly, the cycling stability of the $Li_{0.25}$ material is substantially improved in the first 100 cycles by ethanol rinsing. However, the ethanol rinsed $Li_{0.25}$ material eventually degrades because of the surface reaction and exhibits similar capacity retention (55.9 %) as the untreated material at 250 cycles. In contrast to the undoped material, the addition of the ALD coating to the ethanol rinsed $Li_{0.25}$ material results in a superior 79.9 % capacity retention at 250 cycles. This aligns with the previously displayed failure of the unrinsed, ALD coated $Li_{0.25}$ material beyond 30 cycles being caused by the incomplete protection of the surface caused by the presence of residual sodium species. The ethanol rinsing allows the surface to be more completely coated, providing superior protection compared to direct coating of the pristine powder. Therefore, the ALD coating can stabilize the surface of the $Li_{0.25}$ material, while the Na-O3/Li-O'3 intergrowth provides structural stability. The combined stability of the surface and bulk in ALD coated $Li_{0.25}$ results in long term cycling stability.

Overall, we find that Li promotes the reactivity of the surface by forming an unstable CEI, which is the limiting factor for the cycling performance of these NFM-Li_y materials. However, the addition of Li provides mechanical reinforcement during cycling via the Na-O3/Li-O'3 intergrowth that can provide stability over the initial cycles. These intergrowth structures are a valuable tool to prevent detrimental phase transformations. The combination of inert surface coatings with layered-layered intergrowth structures is a promising avenue for the continued development of high-performance positive electrode materials for sodium ion batteries.

3. Conclusions

Systematic variation of Li content in NFM-Li_y was conducted to identify its role in the structural modification and electrochemical performance. Li contents of 0.15 and greater generate a layered/layered Na-O3/Li-O'3 intergrowth structure. XRD and NPD identify that larger fractions of the Li-O'3 phase and shrinking of both structures unit cells are promoted by higher Li contents. The NPD suggests ordering of the transition metal elements, which as EXAFS fitting suggests is associated with the concentration of Ni and Fe in the Li-O'3 phase. XANES shows no change of transition metal oxidation states with Li content, which suggests the formation of residual Na or Li compounds. ^{7}Li and ^{23}Na ssNMR identify that when the total solubility for alkali ions in the layered structure is exceeded, Li continues to form the Li-O'3 phase while the excess Na forms residual sodium compounds such as Na_2O. These residuals provide the charge balance to rationalize the XANES results and may influence the surface reactivity. Higher Li content is associated with improved capacity retention in the initial cycles but also increases the rate of parasitic side reactions that harm the Coulombic efficiency. Operando XRD identified that the capacity retention of $Li_{0.25}$ in the initial cycles results from the superior stability of the mechanically linked Na-O3/Li-O'3 structure, suppressing the P3 to OP2 transition seen in the undoped material. A lower Li content of $Li_{0.10}$ could improve the reversibility of the P3 to OP2 transformation but not fully suppress it, which could allow for accumulated irreversible lattice expansion. HERFD-XANES and XES suggest that the Fe redox mechanism in these samples and multiple other layered oxides does not occur from a transition from the $3d^5$ to $3d^4$ electron configuration, but rather through a shared loss of electron density on the hybridized Fe-O orbitals that does not change the spin state of Fe. The overall Fe redox activity in the NFM-Li_y materials appears minimal and is therefore not associated with the capacity decay as it is at higher Fe contents. The increased rate of side reaction is shown by ex situ ^{23}Na and ^{7}Li ssNMR to be associated with the instability of the CEI, which is the dominant factor in the long-term cycling stability. This can be partially mitigated by ALD coating with alumina after ethanol rinsing, which significantly enhances the capacity retention and Coulombic efficiency. Overall, we find that the layered/layered Na-O3/Li-O'3 intergrowth structure is able to provide structural stability and suppress phase transformation but is overwhelmed by the increased reactivity of the surface if not protected by the inert ALD coating. While the low level of Li doping in $Li_{0.05}$ provides the best performance among these materials, further optimization of coatings, electrolyte formations, the total alkali content, and Na/Li ratio might maintain the stable intergrowth structure and better protect the surface by stabilizing the CEI. This class of layered/layered intergrowth electrode materials is a promising avenue for the development of high-performance sodium ion batteries.

Funding

This material is based upon work supported by the U.S. Department of Energy, Office of Science, Office of Basic Energy Sciences program under Award Number DE-SC0019121. E. Gabriel was supported by the DOE Office of Science Graduate Student Research (SCGSR) program. The SCGSR program is administered by the Oak Ridge Institute for Science and Education (ORISE) for the DOE. ORISE is managed by ORAU under Contract No. DE-SC0014664. K. Graff acknowledges the support by U.S. National Science Foundation (NSF) (grant number DUE-2111549). S. McCallum acknowledges the National Science Foundation (NSF) REU Site: Materials for Society (Award No. 1950305). This research used resources of the Advanced Photon Source and Center for Nanoscale Materials, a DOE Office of Science User Facility operated for the DOE Office of Science by Argonne National Laboratory under Contract DE-AC02-06CH11357, and the Canadian Light Source and its funding partners. Portions of this work were performed at HPCAT (Sector 16), APS, ANL. HPCAT operations are supported by DOE-NNSA's

Office of Experimental Sciences. Work at ORNL's Spallation Neutron Source was sponsored by the Scientific User Facilities Division, Office of Basic Energy Sciences, U.S. Department of Energy. Oak Ridge National Laboratory is managed by UT-Battelle, LLC, for U.S. DOE under Contract No. DEAC05–00OR22725.

CRediT authorship contribution statement

Stephanie McCallum: Investigation. **Julie Pipkin:** Investigation. **Max Cook:** Investigation. **Eungje Lee:** Writing – review & editing, Supervision, Resources, Conceptualization. **Angel Conrado:** Investigation. **Sarah Kuraitis:** Investigation. **Jehee Park:** Resources, Investigation. **Kamila M. Wiaderek:** Writing – review & editing, Resources, Investigation, Data curation. **Andrey Yakovenko:** Resources, Investigation, Data curation. **Changjian Deng:** Investigation, Conceptualization. **Yingying Xie:** Writing – review & editing, Investigation. **Zonghai Chen:** Supervision, Resources. **Shelly D. Kelly:** Writing – review & editing, Supervision, Resources, Methodology, Formal analysis. **Chengjun Sun:** Writing – review & editing, Supervision, Resources, Methodology, Investigation, Formal analysis, Data curation. **Pengbo Wang:** Writing – review & editing, Visualization, Investigation, Formal analysis. **Kincaid Graff:** Investigation. **Eric Gabriel:** Writing – review & editing, Writing – original draft, Visualization, Methodology, Investigation, Formal analysis, Conceptualization. **Yan-Yan Hu:** Writing – review & editing, Supervision, Resources, Formal analysis, Data curation. **Dewen Hou:** Writing – review & editing, Investigation, Formal analysis. **Yuzi Liu:** Writing – review & editing, Supervision, Resources, Data curation. **Elton Graugnard:** Writing – review & editing, Supervision, Resources, Data curation. **Yang Ren:** Resources, Investigation, Data curation. **Yuming Xiao:** Writing – review & editing, Resources, Investigation, Data curation. **Jue Liu:** Writing – review & editing, Resources, Investigation, Data curation. **Cheng Li:** Writing – review & editing, Resources, Investigation, Data curation. **Inhui Hwang:** Writing – review & editing, Investigation. **Hui Xiong:** Writing – review & editing, Supervision, Resources, Project administration, Funding acquisition, Formal analysis, Data curation, Conceptualization.

Declaration of Competing Interest

The authors declare that they have no known competing financial interests or personal relationships that could have appeared to influence the work reported in this paper.

Appendix A. Supporting information

Supplementary data associated with this article can be found in the online version at doi:10.1016/j.nanoen.2024.110556.

Data Availability

Data will be made available on request.

References

[1] X. Liang, J.-Y. Hwang, Y.-K. Sun, Practical cathodes for sodium-ion batteries: who will take the crown? Adv. Energy Mater. 13 (2023) 2301975 https://doi.org/10.1002/aenm.202301975.
[2] E. Gabriel, D. Hou, E. Lee, H. Xiong, Multiphase layered transition metal oxide positive electrodes for sodium ion batteries, Energy Sci. Eng. 10 (2022) 1672–1705, https://doi.org/10.1002/ese3.1128.
[3] J. Deng, W.-B. Luo, S.-L. Chou, H.-K. Liu, S.-X. Dou, Sodium-ion batteries: from academic research to practical commercialization, Adv. Energy Mater. 8 (2018) 1701428, https://doi.org/10.1002/aenm.201701428.
[4] Q. Liu, Z. Hu, M. Chen, C. Zou, H. Jin, S. Wang, S.-L. Chou, Y. Liu, S.-X. Dou, The cathode choice for commercialization of sodium-ion batteries: layered transition metal oxides versus prussian blue analogs, Adv. Funct. Mater. 30 (2020) 1909530, https://doi.org/10.1002/adfm.201909530.
[5] C. Delmas, C. Fouassier, P. Hagenmuller, Structural classification and properties of the layered oxides, Phys. BC 99 (1980) 81–85, https://doi.org/10.1016/0378-4363(80)90214-4.
[6] E. Gabriel, C. Ma, K. Graff, A. Conrado, D. Hou, H. Xiong, Heterostructure engineering in electrode materials for sodium-ion batteries: recent progress and perspectives, eScience 3 (2023) 100139, https://doi.org/10.1016/j.esci.2023.100139.
[7] J. Chen, L. Li, L. Wu, Q. Yao, H. Yang, Z. Liu, L. Xia, Z. Chen, J. Duan, S. Zhong, Enhanced cycle stability of Na0. 9Ni0. 45Mn0. 55O2 through tailoring O3/P2 hybrid structures for sodium-ion batteries, J. Power Sources 406 (2018) 110–117, https://doi.org/10.1016/j.jpowsour.2018.10.058.
[8] B. Xiao, X. Liu, M. Song, X. Yang, F. Omenya, S. Feng, V. Sprenkle, K. Amine, G. Xu, X. Li, D. Reed, A general strategy for batch development of high-performance and cost-effective sodium layered cathodes, Nano Energy 89 (2021) 106371, https://doi.org/10.1016/j.nanoen.2021.106371.
[9] X. Qi, L. Liu, N. Song, F. Gao, K. Yang, Y. Lu, H. Yang, Y.-S. Hu, Z.-H. Cheng, L. Chen, Design and comparative study of O3/P2 hybrid structures for room temperature sodium-ion batteries, ACS Appl. Mater. Interfaces 9 (2017) 40215–40223, https://doi.org/10.1021/acsami.7b11282.
[10] E. Lee, J. Lu, Y. Ren, X. Luo, X. Zhang, J. Wen, D. Miller, A. DeWahl, S. Hackney, B. Key, D. Kim, M.D. Slater, C.S. Johnson, Layered P2/O3 intergrowth cathode: toward high power Na-ion batteries, Adv. Energy Mater. 4 (2014) 1400458, https://doi.org/10.1002/aenm.201400458.
[11] S. Guo, P. Liu, H. Yu, Y. Zhu, M. Chen, M. Ishida, H. Zhou, A Layered P2- and O3-type composite as a high-energy cathode for rechargeable sodium-ion batteries, Angew. Chem. Int. Ed. 54 (2015) 5894–5899, https://doi.org/10.1002/anie.201411788.
[12] R. Li, Y. Liu, Z. Wang, J. Li, A P2/O3 biphasic cathode material with highly reversibility synthesized by Sn-substitution for Na-ion batteries, Electrochim. Acta 318 (2019) 14–22, https://doi.org/10.1016/j.electacta.2019.06.020.
[13] Y. Liang, H. Xu, K. Jiang, J. Bian, S. Guo, H. Zhou, A high-stability biphasic layered cathode for sodium-ion batteries, Chem. Commun. 57 (2021) 2891–2894, https://doi.org/10.1039/D0CC08302J.
[14] G.-L. Xu, R. Amine, Y.-F. Xu, J. Liu, J. Gim, T. Ma, Y. Ren, C.-J. Sun, Y. Liu, X. Zhang, Insights into the structural effects of layered cathode materials for high voltage sodium-ion batteries, Energy Environ. Sci. 10 (2017) 1677–1693, https://doi.org/10.1039/C7EE00827A.
[15] Q. Huang, S. Xu, L. Xiao, P. He, J. Liu, Y. Yang, P. Wang, B. Huang, W. Wei, Improving the electrochemical properties of the manganese-based P3 phase by multiphasic intergrowth, Inorg. Chem. 57 (2018) 15584–15591, https://doi.org/10.1021/acs.inorgchem.8b02931.
[16] C. Deng, P. Skinner, Y. Liu, M. Sun, W. Tong, C. Ma, M.L. Lau, R. Hunt, P. Barnes, J. Xu, H. Xiong, Li-substituted layered spinel cathode material for sodium ion batteries, Chem. Mater. 30 (2018) 8145–8154, https://doi.org/10.1021/acs.chemmater.8b02614.
[17] Z. Chenglong, W. Qidi, Y. Zhenpeng, W. Jianlin, S.-L. Benjamín, D. Feixiang, Q. Xingguo, L. Yaxiang, B. Xuedong, L. Baohua, L. Hong, A.-G. Alán, H. Xuejie, D. Claude, W. Marnix, C. Liquan, H. Yong-Sheng, Rational design of layered oxide materials for sodium-ion batteries, Science 370 (2020) 708–711, https://doi.org/10.1126/science.aay9972.
[18] J. Hong, H. Gwon, S.-K. Jung, K. Ku, K. Kang, Review—lithium-excess layered cathodes for lithium rechargeable batteries, J. Electrochem. Soc. 162 (2015) A2447, https://doi.org/10.1149/2.0071514jes.
[19] D. Kim, M. Cho, K. Cho, Rational Design of Na(Li1/3Mn2/3)O2 operated by anionic redox reactions for advanced sodium-ion batteries, Adv. Mater. 29 (2017) 1701788, https://doi.org/10.1002/adma.201701788.
[20] J.B. Goodenough, D.G. Wickham, W.J. Croft, Some magnetic and crystallographic properties of the system Li+xNi+ +1−2xni+ ++xO, J. Phys. Chem. Solids 5 (1958) 107–116, https://doi.org/10.1016/0022-3697(58)90136-7.
[21] M. Bianchini, M. Roca-Ayats, P. Hartmann, T. Brezesinski, J. Janek, There and back again—the journey of LiNiO2 as a cathode active material, Angew. Chem. Int. Ed. 58 (2019) 10434–10458, https://doi.org/10.1002/anie.201812472.
[22] A. Gutierrez, W.M. Dose, O. Borkiewicz, F. Guo, M. Avdeev, S. Kim, T.T. Fister, Y. Ren, J. Bareño, C.S. Johnson, On disrupting the Na+ -Ion/vacancy ordering in P2-type sodium–manganese–nickel oxide cathodes for Na+ -ion batteries, J. Phys. Chem. C. 122 (2018) 23251–23260, https://doi.org/10.1021/acs.jpcc.8b05537.
[23] Z. Lu, R.A. Donaberger, J.R. Dahn, Superlattice ordering of Mn, Ni, and Co in layered alkali transition metal oxides with P2, P3, and O3 structures, Chem. Mater. 12 (2000) 3583–3590, https://doi.org/10.1021/cm000359m.
[24] M.E. Arroyo y de Dompablo, A. Van der Ven, G. Ceder, First-principles calculations of lithium ordering and phase stability on LixNiO2, Phys. Rev. B 66 (2002) 064112, https://doi.org/10.1103/PhysRevB.66.064112.
[25] A. Boulineau, L. Croguennec, C. Delmas, F. Weill, Structure of Li2MnO3 with different degrees of defects, Solid State Ion. 180 (2010) 1652–1659, https://doi.org/10.1016/j.ssi.2009.10.020.
[26] A. Riou, A. Lecerf, Y. Gerault, Y. Cudennec, Etude structurale de Li2MnO3, Mater. Res. Bull. 27 (1992) 269–275, https://doi.org/10.1016/0025-5408(92)90055-5.
[27] J.N. Reimers, E. Rossen, C.D. Jones, J.R. Dahn, Structure and electrochemistry of LixFeyNi1-yO2, Solid State Ion.-. 61 (1993) 335–344, https://doi.org/10.1016/0167-2738(93)90401-N.
[28] P. Scherrer, Nachr Ges wiss goettingen, Math. Phys. 2 (1918) 98–100.
[29] U. Holzwarth, N. Gibson, The Scherrer equation versus the "Debye-Scherrer equation,", 534–534, Nat. Nanotechnol. 6 (2011), https://doi.org/10.1038/nnano.2011.145.

[30] P. Thompson, D.E. Cox, J.B. Hastings, Rietveld refinement of deby-scherrer synchrotron X-ray data from Al2O3, J. Appl. Crystallogr. 20 (1987) 79–83, https://doi.org/10.1107/s0021889887087090.
[31] N. Yabuuchi, K. Kubota, M. Dahbi, S. Komaba, Research development on sodium-ion batteries, Chem. Rev. 114 (2014) 11636–11682, https://doi.org/10.1021/cr500192f.
[32] D. Carlier, M. Ménétrier, C.P. Grey, C. Delmas, G. Ceder, Understanding the NMR shifts in paramagnetic transition metal oxides using density functional theory calculations, Phys. Rev. B 67 (2003) 174103, https://doi.org/10.1103/PhysRevB.67.174103.
[33] D. Wang, C. Xin, M. Zhang, J. Bai, J. Zheng, R. Kou, J.Y. Peter Ko, A. Huq, G. Zhong, C.-J. Sun, Y. Yang, Z. Chen, Y. Xiao, K. Amine, F. Pan, F. Wang, Intrinsic role of cationic substitution in tuning Li/Ni mixing in high-Ni layered oxides, Chem. Mater. 31 (2019) 2731–2740, https://doi.org/10.1021/acs.chemmater.8b04673.
[34] J. Bréger, N. Dupré, P.J. Chupas, P.L. Lee, T. Proffen, J.B. Parise, C.P. Grey, Short- and long-range order in the positive electrode material, Li(NiMn)0.5O2: a joint X-ray and neutron diffraction, pair distribution function analysis and NMR study, J. Am. Chem. Soc. 127 (2005) 7529–7537, https://doi.org/10.1021/ja050697u.
[35] J. Bréger, M. Jiang, N. Dupré, Y.S. Meng, Y. Shao-Horn, G. Ceder, C.P. Grey, High-resolution X-ray diffraction, DIFFaX NMR and first principles study of disorder in the Li2MnO3–Li[Ni1/2Mn1/2]O2 solid solution, J. Solid State Chem. 178 (2005) 2575–2585, https://doi.org/10.1016/j.jssc.2005.05.027.
[36] K. Ado, M. Tabuchi, H. Kobayashi, H. Kageyama, O. Nakamura, Y. Inaba, R. Kanno, M. Takagi, Y. Takeda, Preparation of LiFeO2 with alpha- NaFeO2-type structure using a mixed-alkaline hydrothermal method, J. Electrochem. Soc. 144 (1997) L177, https://doi.org/10.1149/1.1837791.
[37] X. Zeng, G.-L. Xu, Y. Li, X. Luo, F. Maglia, C. Bauer, S.F. Lux, O. Paschos, S.-J. Kim, P. Lamp, Kinetic study of parasitic reactions in lithium-ion batteries: a case study on LiNi0. 6Mn0. 2Co0. 2O2, ACS Appl. Mater. Interfaces 8 (2016) 3446–3451, https://doi.org/10.1021/acsami.5b11800.
[38] C. Deng, E. Gabriel, P. Skinner, S. Lee, P. Barnes, C. Ma, J. Gim, M.L. Lau, E. Lee, H. Xiong, Origins of irreversibility in layered NaNixFeyMnzO2 cathode materials for sodium ion batteries, ACS Appl. Mater. Interfaces 12 (2020) 51397–51408, https://doi.org/10.1021/acsami.0c13850.
[39] U. Bergmann, P. Glatzel, X-ray emission spectroscopy, Photosynth. Res. 102 (2009) 255–266, https://doi.org/10.1007/s11120-009-9483-6.
[40] G.S. Henderson, F.M.F. de Groot, B.J.A. Moulton, X-ray absorption near-edge structure (XANES) spectroscopy, Rev. Mineral. Geochem. 78 (2014) 75–138, https://doi.org/10.2138/rmg.2014.78.3.
[41] E. Lee, D.E. Brown, E.E. Alp, Y. Ren, J. Lu, J.-J. Woo, C.S. Johnson, New insights into the performance degradation of fe-based layered oxides in sodium-ion batteries: instability of Fe3+ /Fe4+ redox in α-NaFeO2, Chem. Mater. 27 (2015) 6755–6764, https://doi.org/10.1021/acs.chemmater.5b02918.
[42] D.D. Yuan, Y.X. Wang, Y.L. Cao, X.P. Ai, H.X. Yang, Improved electrochemical performance of Fe-substituted NaNi0.5Mn0.5O2 cathode materials for sodium-ion batteries, ACS Appl. Mater. Interfaces 7 (2015) 8585–8591, https://doi.org/10.1021/acsami.5b00594.
[43] A.L. Bail, Whole powder pattern decomposition methods and applications: a retrospection, Powder Diffr. 20 (2005) 316–326, https://doi.org/10.1154/1.2135315.
[44] J. Alvarado, C. Ma, S. Wang, K. Nguyen, M. Kodur, Y.S. Meng, Improvement of the cathode electrolyte interphase on P2-Na2/3Ni1/3Mn2/3O2 by atomic layer deposition, ACS Appl. Mater. Interfaces 9 (2017) 26518–26530, https://doi.org/10.1021/acsami.7b05326.
[45] L. Yang, S. Sun, K. Du, H. Zhao, D. Yan, H.Y. Yang, C. Yu, Y. Bai, Prompting structure stability of O3–NaNi0.5Mn0.5O2 via effective surface regulation based on atomic layer deposition, Ceram. Int. 47 (2021) 28521–28527, https://doi.org/10.1016/j.ceramint.2021.07.009.
[46] S. Chu, X. Jia, J. Wang, K. Liao, W. Zhou, Y. Wang, Z. Shao, Reduced air sensitivity and improved electrochemical stability of P2–Na2/3Mn1/2Fe1/4Co1/4O2 through atomic layer deposition-assisted Al2O3 coating, Compos. Part B Eng. 173 (2019) 106913, https://doi.org/10.1016/j.compositesb.2019.106913.
[47] H.V. Ramasamy, P. N. Didwal, S. Sinha, V. Aravindan, J. Heo, C.-J. Park, Y.-S. Lee, Atomic layer deposition of Al2O3 on P2-Na0. 5Mn0. 5Co0. 5O2 as interfacial layer for high power sodium-ion batteries, J. Colloid Interface Sci. 564 (2020) 467–477, https://doi.org/10.1016/j.jcis.2019.12.132.
[48] L. Zheng, L. Li, R. Shunmugasundaram, M.N. Obrovac, Effect of controlled-atmosphere storage and ethanol rinsing on NaNi0.5Mn0.5O2 for sodium-ion batteries, ACS Appl. Mater. Interfaces 10 (2018) 38246–38254, https://doi.org/10.1021/acsami.8b14209.